Research Square

Preprints are preliminary reports that have not undergone peer review.
They should not be considered conclusive, used to inform clinical practice,
or referenced by the media as validated information.

Electron–buffered Substoichiometric Overlayers Enable Tunable Active Sites and Exceptional Stability in Oxidative and Humid Catalytic Conditions

Xiaole Weng

xlweng@zju.edu.cn

Zhejiang University https://orcid.org/0000-0003-2997-571X

Li Xiang

Zhejiang University

Yumin Mao

Zhejiang University

Kexin Cao

Zhejiang Development & Planning Institute

Wenbo Li

East China University of Science and Technology

Xueqing Luo

ZJU-Hangzhou Global Scientific and Technological Innovation Center

Feng Bi

Zhejiang University https://orcid.org/0000-0002-3308-7689

Bowen Han

Zhejiang University

Junqi Zhang

Zhejiang University

Liang Wang

Zhejiang University https://orcid.org/0000-0002-5826-1866

Sheng Dai

East China University of Science and Technology https://orcid.org/0000-0001-5787-0179

Zhongbiao Wu

Zhejiang University https://orcid.org/0000-0003-0182-5971

Article

Keywords: Strong metal–support interaction, Electron–buffered, Substoichiometric overlayers, Pd catalyst, CO oxidation

Posted Date: September 21st, 2026

DOI: https://doi.org/10.21203/rs.3.rs-9157059/v1

License: This work is licensed under a Creative Commons Attribution 4.0 International License. Read Full License

Additional Declarations: There is **NO** Competing Interest.

Abstract

Oxide encapsulation has emerged as a generalizable synthetic strategy for constructing metal–oxide catalytic interfaces with tailored electronic properties and enhanced activities, yet the instability of substoichiometric overlayers under oxidative/humid conditions and the inability to engineer active sites at atomic–scale thicknesses substantially limit mechanistic understanding and rational design of encapsulated catalysts. Here, we establish electron buffering as a fundamental synthetic strategy that concurrently stabilizes the classical H2–reduction–induced substoichiometric overlayer and tailors its surface chemistry. By incorporating cerium as a reversible electron buffer into TiO2–derived substoichiometric matrices, we construct the first binary–metal–oxide overlayers with tunable atomic thickness (1–5 layers) on Pd nanoparticles. The Ce 4f levels reversibly donate or accept electrons to compensate for oxidative electron loss, preserving encapsulation stability while enabling active–site engineering at the atomic–scale. This synthetic design achieves unprecedented catalytic activity and durability, activating CO oxidation at near–zero temperature, and operating for over 150 hours under O2–, H2O– and SO2–containing conditions, whereas non–buffered overlayers rapidly collapse and deactivate within 5 hours.

Introduction

Heterogeneous catalysts operating under realistic reaction environments are routinely exposed to oxidized and/or humid atmospheres, where maintaining both high activity and long–term structural stability is usually a central challenge[1,2]. For supported noble–metal catalysts, interfacial interactions between metals and oxide supports play a decisive role in governing electronic structure, catalytic performance, and durability[3-10]. Among these interactions, encapsulation of metal nanoparticles by reducible oxides has been widely explored as an efficient route to modulate metal reactivity and suppress deactivation, which is described as strong metal–support interactions (SMSIs)[3,11]. However, such encapsulated structures are generally regarded as incompatible with oxidative or humid atmospheres[12,13].

To address the stability limitations of SMSI overlayers under oxidative and humid conditions, recent researches have shifted toward alternative construction strategies distinct from the classical H_2–reduction–induced route. Liu et al.[14], Chen et al.[10], and Tang et al.[15], obtained robust TiO_x overlayers over metal particles through oxidative strong metal–support interaction (O–SMSI), which was stable against the oxidation by O_2 and H_2O. Wang et al.[16] further addressed this challenge by establishing a water–triggered SMSI that maintains structural integrity against oxidation by O_2/H_2O. Matsubu et al.[5] and Li et al.[17] demonstrated CO_2–rich pretreatment with H_2 can induce the formation of strongly bound adsorbates (HCO_x) on reducible oxide–supports, resulting in adsorbate–mediated strong metal–support interaction (A–SMSI) of Rh NPs by the supports that was stable against the re–oxidation by H_2O. However, the realization of classical SMSI overlayers with robust stability and interfacial activity in humid

and oxidative atmospheres remains elusive. Particularly, owing to the atomic–scale thickness, precise compositional and structural engineering of aforementioned overlayers is extraordinarily challenging and has rarely been achieved. This constraint reflects the inherent thermodynamic and kinetic barriers to active site engineering at overlayers, substantially limiting mechanistic understanding and rational design of encapsulated catalysts.

Here, we report the first realization of compositional and structural engineering of substoichiometric overlayers through secondary metal cation incorporation and atomic–scale thickness control. Recognizing that overlayer collapse is commonly triggered by electron extraction from adsorbed O_2 and H_2O[3,16,18], we establish an electron–buffered strategy by integrating electron–buffering elements directly into the substoichiometric overlayer matrix. This design compensates for electron loss, preserving the essential electronic force for encapsulation stability by sustaining interfacial electron transfer from the overlayer to encapsulated metal[3,11,19,20]. Cerium serves as an ideal electron buffer: its Ce 4f levels can rapidly and reversibly donate or accept electrons to and from the O_2 π* manifold, thereby storing and releasing electrons without permanent Fermi level shift[21]. We therefore introduce Ce into a TiO_2–derived substoichiometric oxide matrix and induce encapsulation under classical H_2 reductive treatment to construct a Ce–Ti binary–metal–oxide overlayer with tunable thickness (1–5 atomic layers) on Pd nanoparticles. This engineering establishes intrinsic electron–buffered capability within the overlayer, which not only significantly boosts catalytic activity in carbon monoxide (CO) oxidation, but also enables classical substoichiometric overlayer to operate stably for the first time under oxidative and humid conditions, even in the presence of SO_2 as a potent poison for over 150 hours, whereas Ce–free substoichiometric overlayers rapidly collapse and deactivate within 5 hours. More broadly, Ce–Ti encapsulation is extendable to other precious metals such as Au and Pt and the electron–buffering principle proves applicable across other alternative buffers (*e.g.*, Sn), providing a fundamental design strategy for engineering atomically defined overlayers with durable active sites operable under realistic reaction conditions.

Results

Stable electron–buffered substoichiometricoverlayer

We first used a continuous hydrothermal flow reactor to obtain highly dispersed and strongly interacted $Pd/CeTiO_x$nanoparticles (NPs) to facilitate subsequent encapsulation[22] (Supporting Information, **Fig. S1**). During the synthesis (**Fig. 1a**), Pd salts were rapidly co–precipitated with the metal salts of Ce and Ti (Ce–to–Ti molar ratio at 1:1) under a supercritical water (sc–H_2O) condition (T_c = 374.3 ^oC, P_c = 22.1 MPa). The yielded $Pd/CeTiO_x$ NPs were subsequently reduced in a 5 vol% hydrogen atmosphere at 400 ^oC for 4 hours. The resulting sample was hereafter denoted as $Pd/CeTiO_x$–H. Benchmark controls (Pd/TiO_2–H and Pd/CeO_2–H) were fabricated identically except for the use of metal salts. Inductively coupled plasma optical emission spectrometry (ICP–OES) confirmed that Pd

loadings were in the narrow range of 0.85–0.95 *wt*% for all samples, and Ce–to–Ti molar ratio was about 1.03:1 for Pd/$CeTiO_x$–H (**Table S1**). X–ray powder diffraction (XRD) patterns of Pd/TiO_2–H and Pd/CeO_2–H closely matched the standard JCPDS reference for brookite TiO_2 (JCPDS pattern number 46–1237; Supporting Information, **Fig.S2a**) and fluorite cubic CeO_2 (JCPDS pattern number34–0394; Supporting Information, **Fig.S2b**), respectively, with no detectable diffraction peaks corresponding to Pd species. While for Pd/$CeTiO_x$–H, the diffraction pattern exhibited a feature of mixed $CeTiO_x$ phases (Supporting Information, **Fig. S2c**). Moreover, the Brunauer–Emmett–Teller surface areas (S_{BET}) of Pd/CeO_2–H, Pd/TiO_2–H, and Pd/$CeTiO_x$–Hexhibited approximately 100.6, 102.4 and 107.7 $m^2\ g^{-1}$, respectively (**Table S1**).

The encapsulated structures between Pd and oxide supports after H_2 treatment were probed using aberration–corrected transmission electron microscopy (AC–TEM). As shown in **Fig. 1b** and **e**,thePd/TiO_2–H and Pd/$CeTiO_x$–H contained Pd NPs with an average size of ~9.5 nm and ~3.8 nm, respectively, and the Pd NPs were covered by the overlayers. Electron energy loss spectroscopy (EELS) analysis was performed to probe the structural composition and elemental chemical state of the overlayers. As illustrated in **Fig.S3**, the Ti L–edge EELS spectrum of the overlayers exhibited four distinct peaks, labeled a, b, c, and d. The first doublet at lower energy loss comprises the Ti L_3 edge, and the second at a higher energy loss comprises the Ti L_2 edge. The fine structures are known to be sensitive to the valence state, coordination environment, and site symmetry of the Ti species[23]. The EELS analyses confirmed the presence of Ti^{3+} and Ti^{4+} in the binary–metal–oxide overlayer of Pd/$CeTiO_x$–H, which was different from the classical SMSI scenarios (herein the Pd/TiO_2–H) that Ti^{3+} species dominate[24]. Ce EELS spectra were characterized by sharp white lines of $3d_{3/2}\rightarrow4f_{5/2}$ (M_4) at 901 eV and $3d_{5/2}\rightarrow4f_{7/2}$ (M_5) at 883 eV associated with the spin–orbit split. Generally, Ce^{3+} exhibits the M_4/M_5 value at 0.78 in orthophosphate, and Ce^{4+} is at 1.10 in CeO_2[25-27]. While for the Pd/$CeTiO_x$–H, the M_4/M_5 value was 1.08, suggesting a dominant Ce^{4+} state in the overlayer, and the Ce–to–Ti ratio was measured at about 3:7 (based on EELS element quantification)[28]. Moreover, the thickness of the binary–metal–oxide overlayer was measured at about 0.4–1.0 nm, corresponding to approximately 2–5 atomic layers.

CO–adsorption diffuse reflectance infrared Fourier transform spectroscopy (CO–DRIFTS) was also conducted to confirm the encapsulated structure. The Fourier Transform Infrared (FTIR) spectra of Pd/CeO_2 and Pd/TiO_2 initially treated at 400 ℃ with H_2 showed broad peaks at 2071–2087 and 1950–1972 cm^{-1}, corresponding to the physically adsorbed CO on $Pd^{\delta+/0}$ and chemically adsorbed CO on metallic Pd^0, respectively (Supporting Information, **Fig.S4**)[29]. However, these peaks were not observed in the Pd/$CeTiO_x$–H (Supporting Information, **Fig.S5a**), indicating the formation of an encapsulation overlayer on the Pd. Upon further increasing the reduction temperature to 500 ℃, a classical overlayer structure emerged in Pd/TiO_2–H (Supporting Information, **Fig.S5b**), whereas no such encapsulation was observed for Pd/CeO_2–H. Generally, a large difference in work function between metals and

supports can favour the formation of oxide overlayers[11]. Therefore, the lower H_2 reduction temperature for Pd/$CeTiO_x$–H could arise from its decreased work function of $CeTiO_x$ compared to individual TiO_2 and CeO_2. Indeed, as calculated using density functional theory (DFT), the work functions of $CeTiO_x$ with varied configurations (3.60–4.47 eV) were all shown distinctly lower than those of TiO_2 (7.38 eV) and CeO_2 (7.80 eV) (Supporting Information, **Fig. S6–S9**).

To evaluate the stability of the unary– and binary–metal–oxide overlayers, the encapsulated samples were then subjected to calcination under humid air (20 vol% O_2 and 5 vol% H_2O) at 200 ^oC, a condition known to readily retreat the substoichiometric oxide overlayers of classical SMSIs[5]. As shown in**Fig. S5b**, the encapsulated structure of Pd/TiO_2–H disintegrated after humid–air treatment, as evidenced by the reappearance of linear CO adsorption bands associated with $Pd^{\delta+/0}$ sites in the treated Pd/TiO_2–H. Consistent with this observation, TEM and energy–dispersive X–ray spectroscopy (EDS) mapping analysis revealed exposed Pd nanoparticles with undetected oxide overlayers (**Fig. 1c** and **d**), confirming overlayer retreat–off under oxidative and humid conditions, in agreement with previous results[12]. In contrast, the encapsulated structure of Pd/$CeTiO_x$–H remained intact after treatment in an oxidative and humid atmosphere, as demonstrated by the TEM imaging, EDS mapping, and CO–DRIFTS (**Fig. 1f**, **1g** and **Fig. S5a**). To the best of our knowledge, this represents the first example of a classical H_2–reduction–induced substoichiometric overlayer structure that remains stable under oxidative and humid conditions. Further CO–DRIFTS analysis confirmed that this binary–metal–oxide overlayer was also stable even up to 1 vol% O_2 and 15 vol% H_2O at 300 ^oC (Supporting Information, **Fig.S5a**).

Dynamic formation of electron–buffered substoichiometricoverlayer

We further performed *in situ* environmental TEM study to directly probe the formation process of overlayer on the Pd nanoparticles[30]. As shown in **Fig. 2a–c**, Pd NPs with an average size of ~5 nm loaded on $CeTiO_x$ were initially uncovered. Upon reduction at 400 ^oC under 5 vol% hydrogen environment for 30 minutes, an amorphous encapsulation emerged at the Pd–$CeTiO_x$ interface. With prolonged reduction, a continuous overlayer fully developed after 60 min (marked by yellow rectangles). The Ti L–edge and Ce M_4/M_5–edge EELS spectra revealed that Ti and Ce were predominantly in the Ti^{4+} and Ce^{4+} states in the *in situ* formed overlayer, respectively (Supporting Information, **Fig. S7–S10**). The M_4/M_5 intensity ratio derived from the Ce M_4/M_5–edge EELS spectrum was 1.04, lower that in the Pd/$CeTiO_x$–H (1.08), suggesting air exposure had slightly oxidized the binary–metal–oxide overlayer, while the Ce–to–Ti ratio remained at approximately 3:7.

To probe chemical valence changes during H_2 reduction, *in situ* near–ambient pressure X–ray photoelectron spectroscopy (NAP–XPS) analysis was performed on Pd/$CeTiO_x$ at 400 °C under H_2 purge. As shown in **Fig.S11a**, the fraction of Pd^{2+} decreased markedly upon H_2 exposure, while that of Pd^0 increased from 0.10 to 0.45, indicating the onset of Pd encapsulation accompanied by electron

donation from the oxide overlayer[31]. After H_2 purging for 60 min, the fraction of Ce^{3+} decreased from 0.44 to 0.25, reflecting electron loss from Ce during the encapsulation (Supporting Information, **Fig.S11b**)[32]. In contrast, the Ti 2p spectra (Supporting Information, **Fig.S11c**) showed no discernible shoulder peaks between 455.8 and 456.7 eV, excluding the formation of reduced Ti species[33]. Notably, a slight shift of Ti 2p peaks toward lower binding energy was observed, suggesting electron transfer from Ce to Ti upon H_2 reduction. Furthermore, O 1s spectra revealed a gradual decrease in chemisorbed oxygen (O_{ads}) at 530.8 eV from 0.19 to 0.09 during H_2 treatment[34], which could be attributed to the increased Ce^{4+} content in the Pd/$CeTiO_x$–H (Supporting Information, **Fig.S12**). To distinguish the effect of H_2 reduction on the electronic states of Ce and Ti in bulk $CeTiO_x$ from that at the metal–oxide interface, *in situ* NAP–XPS of Pd–free $CeTiO_x$ was performed, which revealed an increase in Ce^{3+}, Ti^{3+} and O_{ads} contents under H_2 atmosphere, distinctly differing from the Pd/$CeTiO_x$–H. This observation further confirmed that electron donation from Ce to Pd during H_2–reduction–induced encapsulation (Supporting Information, **Fig. S13**).

The Pd K–edge X–ray absorption spectroscopy (XAS) results for Pd/TiO_2–H, Pd/$CeTiO_x$–H, Pd foil, and PdO are shown in **Fig. 2d–f**. From the normalized X–ray absorption near–edge structure (XANES) (**Fig. 2d**), the absorption edge positions of both Pd/TiO_2–H and Pd/$CeTiO_x$–H were located between those of the PdO and Pd foil, indicating that Pd species in both samples possessed oxidation states between 0 and +2. Notably, Pd/$CeTiO_x$–H with binary–metal–oxide overlayer exhibited an edge position closer to that of Pd foil compared to TiO_x–encapsulated Pd/TiO_2–H. The spectra of corresponding extended X–ray absorption fine structure (EXAFS) in R–space are given in **Fig. 2e**, **Fig. S14**and **S15**, showing two prominent peaks at ~1.5 and ~2.5 Å that can be attributed to Pd–O and metallic Pd–Pd bonding, respectively. The coordination numbers of Pd–O were calculated to be 2.5 and 2.3, with an average bond distance of 2.00 and 2.04 Å over Pd/TiO_2–H and Pd/$CeTiO_x$–H, respectively (**Table S2**), further substantiating the decreased Pd valence state induced by $CeTiO_x$ overlayer. Wavelet transform (WT) analysis of EXAFS provided enhanced resolution in both k–space and R–space, enabling precise discrimination of coordination conditions (**Fig. 2f**). The WT EXAFS contour plots of Pd/TiO_2–H and Pd/$CeTiO_x$–H both exhibited a maximum intensity peak of Pd–O path (~4.80 $Å^{-1}$ in k–space and ~1.49 Å in R–space) with a weak peak of Pd–Pd path (~7.20 $Å^{-1}$ in k–space and ~2.52 Å in R–space), consistent with partially metallic Pd species (Supporting Information, **Fig.S16**)[35].

Electron–buffered mechanism for stable substoichiometric overlayer

We first evaluated the oxygen storage capacity (OSC) of Pd/$CeTiO_x$–H and Pd/TiO_2–H. As shown in **Fig. 3a**and**Fig. S17**, the Pd/$CeTiO_x$–H yielded an OSC value at 428 μmol/g_{cat}, which was about 8–fold that of Pd/TiO_2–H (50 μmol/g_{cat}), confirming the function of Ce doping into the TiO_2 overlayer in efficiently restoring resistance to O_2 attack. To elucidate the interfacial charge transfer behaviors between encapsulated metal and oxide overlayer, density functional theory (DFT) calculations were then

performed. The palladium surface was modeled as a four–layer Pd(111) slab containing 16 Pd atoms per layer[10]. The TiO_2–encapsulated models with two layers were constructed with slabs containing 18 Ti and 36 O atoms[36]. Because a random solid solution is impractical for periodic Vienna Ab–initio Simulation Package (VASP) calculations, an approximate $CeTiO_x$–encapsulated model was constructed based on the metal–site occupancies and the overall Ce:Ti ratio set at 3:7 as indicated by EELS analyses[37]. We acknowledged the inherent limitations of using periodic crystalline models to simulate experimentally observed amorphous structures. Accordingly, the DFT simulations in this work served mainly to elucidate qualitative trends in electronic structure modulation and interfacial charge redistribution, rather than to provide atomically precise reconstruction or quantitative prediction of the experimental amorphous overlayer under real reaction conditions.

As shown in **Fig.S18**, DFT calculations revealed a strong tendency for Ce to segregate to the surface of Ce–Tioverlayer, as a clear stabilization of the structure when Ce occupied the surface site compared to the core region. For encapsulated $Pd@Ti_{18}O_{36}$ and $Pd@Ce_5Ti_{13}O_{36}$ models, electron transferred from the overlayer to Pd metal (**Fig. 3b)**, which was consistent with the *in situ* NAP–XPS and EXAFS results. However, following the adsorption of O_2 and H_2O, electron transfer remained exclusively from the $Ce_5Ti_{13}O_{36}$ overlayer to Pd metal, in contrast to the reverse direction seen in $Ti_{18}O_{36}$ overlayers (**Fig. 3b** and **Fig. S19–S21**). The projected density of states (PDOS) provided further insights into the electronic information. As shown in **Fig. S22**, upon H_2O or O_2 adsorption on the encapsulated $Pd@Ce_5Ti_{13}O_{36}$ model, the electronic contribution from Ce 4f state diminished while that from Pd 4d state increased, with Ti 3d states exhibiting only limited variation, indicating an electron density shift from Ce 4f to Pd 4d orbital. Concurrently, crystal orbital Hamilton population (COHP) analysis revealed that the positive contribution of Pd–Ce bonding below the Fermi level intensified upon H_2O or O_2 adsorption (**Fig. 3c** and **Fig. S23**), signifying strengthened orbital interaction at the Pd–Ce interface. This indicated that the introduction of Ce induced a prominent "electron–buffered" effect at the interface. Moreover, the proposed electron–buffering effect was experimentally supported by EELS and EXAFS analyses on post–treatment $Pd/CeTiO_x$–H (Supporting Information, **Fig. S24, S25,** and **Table S2**). A slightly increased Ce EELS M_4/M_5 ratio (from 1.08 to 1.09), a Pd K–edge shifted toward Pd foil, and a reduced Pd–O coordination number (from 2.3 to 2.1) all confirmed the electron transfer from Ce to Pd under humid air treatment. In line with the DFT results, these findings confirmed that Ce induced an electron–buffering effect that stabilized the Pd state and maintained encapsulation integrity under oxidative and humid atmospheres. Notably, adsorption of an additional O_2 molecule on the $Ce_5Ti_{13}O_{36}$ overlayer induced reversal of electron transfer in the encapsulated $Pd@Ce_5Ti_{13}O_{36}$ model (Supporting Information, **Fig. S26**). This computationally predicted behavior aligned with the experimentally observation, in which $Pd/CeTiO_x$–H can resist up to 1 vol% O_2 and 15 vol% H_2O at 300 ^oC, but overlayer retreat–off occurred under 20 vol% O_2 and 5 vol% H_2O at 250 ^oC or 80 vol% O_2 and 5 vol% H_2O at 200 ^oC (Supporting Information, **Fig. S27**), indicating that the electron–buffering effect operates within a defined thermodynamic limit.

Atomic–scale thickness tuning ofelectron–buffered substoichiometricoverlayer

To tune the atomic–scale thickness of oxide overlayers, an additional sample was prepared via wet impregnation of the $(NH_4)_2PdCl_6$ onto sc–H_2O–derived $CeTiO_x$, followed by a reduction at 400 °C for 4 h in H_2 (denoted as Pd/$CeTiO_x$–IM, Supporting Information, **Fig.S28**). We proposed that impregnated Pd remains on the $CeTiO_x$surface with minimal lattice incorporation, exhibiting limited mobility and weaker metal–support interaction compared to sc–H_2O–derived Pd/$CeTiO_x$–H, thereby suppressing $CeTiO_x$oxide spreading and yielding atomically thinner overlayer. Indeed, TEM analysis showed that the Pd/$CeTiO_x$–IM contained an overlayer with a thickness of 0.2–0.4 nm, corresponding to only 1–2 atomic layers (Supporting Information, **Fig.S29a**). The OSC measurements revealed a lower value for Pd/$CeTiO_x$–IM (177 μmol/g_{cat}) compared to Pd/$CeTiO_x$–H (428 μmol/g_{cat}), indicating decreased resistance ability to O_2 attack (**Fig. 3a** and **Fig.S17**). EELS analyses revealed a higher Ce content in the overlayer of Pd/$CeTiO_x$–IM, consisted of Ce–to–Ti ratio at 45:55, accompanied by a reduced M_4/M_5 ratio of 0.86 compared to 1.08 for Pd/$CeTiO_x$–H, indicating the presence of a higher fraction of Ce^{3+} species (Supporting Information, **Fig.S29c**and**d**). *In situ* NAP-XPS also confirmed the onset of Pd encapsulation accompanied by electron donation from the oxide overlayer (Supporting Information, **Fig.S30 and S31**).

Upon calcination in humid air (20 vol% O_2 and 5 vol% H_2O) at 200 ^oC, the thin binary–metal–oxide overlayer in the Pd/$CeTiO_x$–IM disintegrated, as evidenced by the reappearance of linear CO adsorption bands on $Pd^{\delta+/0}$ sites (Supporting Information, **Fig.S28**). DFT calculations for a case of one–layer $Ce_4Ti_5O_{18}$ showed reversed electron transfer from Pd to the oxide overlayer upon O_2 and H_2O adsorption (Supporting Information, **Fig. S32** and **S33**), confirming that insufficient electron–buffering capacity led to overlayer destabilization. To further decouple the thickness effect, a monolayer encapsulation model Pd@$Ce_3Ti_6O_{18}$ with a Ce fraction comparable to that of Pd@$Ce_5Ti_{13}O_{36}$ was constructed (Supporting Information, **Fig. S34**). Similarly, electron transfer from Pd to the oxide overlayer was observed upon O_2 and H_2O adsorption on Pd@$Ce_3Ti_6O_{18}$ (Supporting Information, **Fig. S35**), further underscoring the critical role of overlayer thickness (referring to the electron buffered capability) in stabilizing the encapsulated structure under oxidative and humid conditions. Collectively, the strong interaction between Pd and an electron–buffered Ce–Ti overlayer enables sustained electron exchange at the interface, thereby stabilizing the encapsulated structure under oxidative and humid conditions (**Fig. 3d**).

Catalytic performanceof electron–buffered substoichiometricoverlayer

The carbon monoxide (CO) oxidation light–off curves were measured to evaluate the catalytic activities. As shown in **Fig. 4a**, Pd/$CeTiO_x$–H achieved complete CO conversion at a low temperature of ~20 °C, with an apparent activation energy (E_a) of 38.3 kJ/mol (Supporting Information, **Fig.S36**). Notably, after increasing the gas hourly space velocity of 200,000 mL $gcat^{-1}$ $hour^{-1}$(gcat, grams of catalyst), the T_{100} of CO oxidation retained at ~120 °C, meeting the standard of “The 150 °C Challenge”[38]. Even after

100 consecutive CO oxidation cycles, Pd/$CeTiO_x$–H still meet this standard, with the encapsulation structure remaining largely intact (Supporting Information, **Fig. S37**–**S39**).

On unencapsulated Pd/CeO_2 and Pd/TiO_2 catalysts, CO oxidation proceeds via CO adsorption on Pd sites, reaction of adsorbed CO and lattice oxygen, and vacancy replenishment by gas-phase O_2 dissociation[39,40]. However, CO was inaccessible to Pd sites in the encapsulated Pd/$CeTiO_x$–H catalyst, as confirmed by the complete absence of CO adsorption peaks in CO–DRIFTS (Supporting Information, **Fig. S5**). Our DFT calculations thus identified the bridging lattice oxygen of the Ce–O–Ti in the overlayer as the preferential CO adsorption site, with CO adopting a C–end configuration. This adsorbed CO subsequently abstracted the lattice oxygen to form CO_2, which desorbed and left behind an oxygen vacancy (**Fig. 4b**).

To determine whether the oxygen vacancy formed after CO oxidation underwent redistribution to the surrounding environment, we calculated the vacancy formation energy of the Ce–O–Ti site involved in CO oxidation and compared it with those of three adjacent sites (Supporting Information, **Fig. S40**). The results showed that the Ce–O–Ti site participating in CO oxidation exhibited the lowest vacancy formation energy. This finding indicated that subsequent vacancy regeneration did not rely on long–range oxygen migration, but rather on oxygen dissociation in the vicinity of the original reaction site. We therefore further calculated the O_2 dissociation process at the Ce–O_v–Ti site. Because the O_2 dissociation at the asymmetric Ce–O_v–Ti vacancy site was jointly influenced by the local structures of Ce and Ti, Ti–assisted and Ce–assisted O_2 dissociation pathways were further calculated and compared. The Ce–assisted pathway was kinetically and thermodynamically superior, with only 0.47 eV of energy barrier for O–O cleavage following spontaneous intermediate formation, compared with 1.33 eV for the Ti–assisted pathway. The final–state energy of the Ce–assisted pathway (–1.94 eV) was also markedly lower than that of the Ti–assisted pathway (–1.27 eV). Upon complete O_2 scission, one oxygen atom replenished the vacancy while the other served as a surface oxygen species for subsequent reaction. These results demonstrated that the Ce–O–Ti bridging site functions as the active center for CO oxidation, with Ce playing a critical role in facilitating O_2 activation and vacancy regeneration. CO temperature–programmed reduction (CO–TPR) analyses further verified this exceptional oxygen reactivity, showing markedly lower reduction peaks for the Ce–O–Ti in Pd/CeTiO□–H compared to that in unencapsulated Pd/$CeTiO_x$ (Supporting Information, **Figure S41**).

Under realistic conditions, SO_2 widely coexists with CO in the exhausts from vehicles, heating boilers, metallurgy, iron and steel sintering, and solid waste co–incineration[41-43], and is a potent poison for noble–metal catalysts[44]. To validate the shell–protection function of electron–buffered $CeTiO_x$ overlayer in preventing the SO_2 poisoning of Pd cores, we examined the potential of Pd/$CeTiO_x$–H in sustaining SO_2, H_2O, and O_2–containing feed at various temperatures and SO_2 concentrations. As shown in **Fig.S42**,Pd/$CeTiO_x$–H demonstrated excellent stability under SO_2 and O_2–containing feed at 200°C, maintaining 100% activity in CO oxidation after 80 hours of testing, while the PdCeTiO_x–IM and Pd/TiO_2–

H decreased activity to below 70% after 5 hours. Moreover, adding 5 vol% H_2O into the SO_2 and O_2–containing feed, the Pd/$CeTiO_x$–H was shown to maintain 100% activity in CO oxidation for 100 hours (Supporting Information, **Fig.S43**).

After decreasing the durability test temperatures to 125 and 150 °C, the Pd/$CeTiO_x$–H showed robust H_2O tolerance, whereas an obvious deactivation was observed upon the addition of SO_2 (**Fig. 4c**). However, when the temperature was elevated to 175 °C, Pd/$CeTiO_x$–H exhibited robust resistance to both SO_2, O_2 and H_2O attack, showing a slight loss of activity to 85% in CO oxidation even after 25 hours of exposure to 1000 ppm SO_2. Notably, its activity can be fully restored upon the removal of SO_2, suggesting a reversible deactivation feature for SO_2 attack. This reversibility was further confirmed by extended SO_2 durability tests, whereas complete performance recovery was observed in each of the four cycles upon switching off SO_2 (Supporting Information, **Fig.S44**). Such sustained high activity under the conditions containing SO_2, H_2O, and O_2 has rarely been reported for Pd–based catalysts[38], underscoring the exceptional stability conferred by the unique electron–buffered binary–metal–oxide overlayer. Further SO_2–FTIR analysis (Supporting Information, **Fig.S45a**) revealed that, although Ce–related tridentate sulfates accumulated abundantly on Pd/$CeTiO_x$–H upon SO_2 exposure, no sustained sulfate buildup occurred after prolonged testing, as confirmed by the absence of sulfate signals in the FTIR spectra of the spent catalyst[45]. This indicated that partial sulfate accumulation modified the local electronic environment and suppressed further sulfation[29]. Therefore, the reversible activity recovery observed upon SO_2 switching could be ascribed to competitive adsorption between CO and SO_2, which was further validated by comparative investigation of CO–TPD and CO+SO_2–TPD measurements (Supporting Information, **Fig.S45b**). TEM analyses were further performed on the reacted Pd/$CeTiO_x$–H and Pd/$CeTiO_x$–IM catalysts. As shown in **Fig.S46**, the Pd/$CeTiO_x$–H retained its overlayer after reaction, whereas the overlayer on Pd/$CeTiO_x$–IM was no longer observable. Consistent with this structural evolution, no additional CO–FTIR features emerge on the surface of Pd$CeTiO_x$–H after reaction, indicating the well–maintained overlayer. In contrast, Pd$CeTiO_x$–IM exhibited two major CO adsorption bands at 1990 and 1924 cm^{-1}(Supporting Information, **Fig.S47**), characteristic of exposed Pd sites. These findings confirmed that the overlayer structure of Pd/$CeTiO_x$–H remained highly stable after CO–oxidation and can efficiently protect the Pd cores even in the presence of SO_2 potent poison.

Discussion

This work establishes electron–buffered overlayers as a fundamental concept for stabilizing classical H_2–reduction–induced substoichiometric oxide encapsulation under oxidative and humid conditions. By engineering Ce–Ti binary–metal–oxide overlayers with atomically tuned thickness (1–5 atomic layers), we demonstrate that intrinsic electron–buffering capacity governs the stability of encapsulated Pd catalysts under O_2– and H_2O–containing feeds. The reversible Ce^{4+}/Ce^{3+} redox couple enables the

substoichiometric overlayer to dynamically sustain interfacial electron donation to Pd even under oxidative electron depletion, thereby extending encapsulation stability into reaction regimes previously considered inaccessible. The engineered overlayer not only enables classical SMSI structures to operate stably for the first time under oxidative and humid conditions, but also significantly boosts catalytic activity in CO oxidation, even in the presence of SO_2 as a potent poison.

More broadly, Ce–Ti encapsulation can be extended to other precious metals (e.g., Au, Pt; Supporting Information, **Fig. S48** and **S49**) and the electron–buffering principle proves applicable across other alternative buffers (e.g., Sn; Supporting Information, **Fig. S50**–**S53**). To further verify that the stability of the binary–metal–oxide overlayer originates from electron buffering, we additionally synthesized $Pd/ZrTiO_x$, wherein Zr lacks electron–buffering capability. The rapid dissipation of the $ZrTiO_x$ overlayer under humid air further underscores that electron buffering is the primary factor governing overlayer preservation under oxidative and humid conditions (Supporting Information, **Fig. S54**). Furthermore, conventional hydrothermal synthesis of $Pd/CeTiO_x$ can also yield encapsulated catalysts, but with larger Pd particle sizes, thicker overlayers, and substantially lower CO oxidation activity, highlighting the critical role of the supercritical hydrothermal approach in achieving a highly active encapsulation architecture (Supporting Information, **Fig. S55**–**S57**). Our findings redefine the stability limits of classical H_2–reduction–induced substoichiometric oxide–encapsulated catalysts and establish an electron–buffering–integrated design strategy for engineering durable encapsulated active sites operable under realistic reaction conditions.

Methods

The details of materials are summarized in Supplementary Information section 1. The details of catalyst preparation are summarized in Supplementary Information section 2. The procedures of catalyst characterization conducted for this study are described in Supplementary Information section 3. The details of catalytic tests are summarized in Supplementary Information section 4. Finally, details about the Density Functional Theory (DFT) modeling approach are provided in Supplementary Information section 5.

Declarations

Data Availability

The data that support the findings of this study are available within the paper and its Supplementary information. Source data of Figs. 2–4 are provided with this paper as a Source Data file. Atomic coordinates of the optimized structure of Fig. 3b are provided in Supplementary Data. Extra data are available from the corresponding author on reasonable request. Source data are provided with this paper.

Acknowledgments

We gratefully acknowledge the National Natural Science Foundation of China (525B2164, 22176169, and 22376062), the National Key R&D Program of China (2023YFC3707503), the Postdoctoral Fellowship Program of CPSF (GZB20250303), the Science and Technology Commission of Shanghai Municipality (24DX1400200 and 22ZR1415700), and the Key R&D Plan of Zhejiang Province (2023C03127). We also appreciate the BL14W1 station in Shanghai Synchrotron Radiation Facility (SSRF) for the collection of X–ray absorption spectroscopy data.

Author Contributions

L.X. and K.X.C. carried the experiments and analyzed the results. Y.M.M. and W.B.L. performed the catalyst characterization. X.Q.L. and F.B. collected and analyzed the XAFS data. B.W.H and J.Q.Z supported in assisting with interpreting some of the analytical data and assisting in writing the manuscript. X.L.W., L.X., and K.X.C. conceived the idea and wrote the paper. L.W., S.D., and Z.B.W. supervised the project. All authors discussed the results and assisted during manuscript preparation.

Competing Interests

The authors declare that they have no competing interests.

References

1. Tao, F. & Salmeron, M. Surface restructuring and predictive design of heterogeneous catalysts. *Science* **386**, eadq0102 (2024).
2. Martín, A., Mitchell, S., Mondelli, C., Jaydev, S. & Pérez-Ramírez, J. Unifying views on catalyst deactivation. *Nature Catalysis* **5** (2022).
3. Tauster, S. J., Fung, S. C., Baker, R. T. K. & Horsley, J. A. Strong interactions in supported-metal catalysts. *Science* **211**, 1121-1125 (1981).
4. Chen, S. *et al.* Defective TiO_x overlayers catalyze propane dehydrogenation promoted by base metals. *Science* **385**, 295-300 (2024).
5. Matsubu, J. C. *et al.* Adsorbate-mediated strong metal–support interactions in oxide-supported Rh catalysts. *Nature Chemistry* **9**, 120-127 (2017).
6. Li, Y., Zhang, Y., Qian, K. & Huang, W. Metal–support interactions in metal/oxide catalysts and oxide–metal interactions in oxide/metal inverse catalysts. *ACS Catalysis* **12**, 1268-1287 (2022).
7. Tang, H. *et al.* Strong metal–support interactions between gold nanoparticles and nonoxides. *Journal of the American Chemical Society* **138**, 56-59 (2016).
8. Fan, S. *et al.* Subsurface Ru-triggered hydrogenation capability of TiO_{2-x} overlayer for poison-resistant reduction of N-heteroarenes. *ACS Catalysis* **13**, 757-765 (2023).
9. Otor, H. O., Steiner, J. B., García-Sancho, C. & Alba-Rubio, A. C. Encapsulation methods for control of catalyst deactivation: A review. *ACS Catalysis* **10**, 7630-7656 (2020).

10. Chen, J. *et al.* Palladium encapsulated by an oxygen-saturated TiO_2 overlayer for low-temperature SO_2-tolerant catalysis during CO oxidation. *Angewandte Chemie International Edition* **62**, e202310191 (2023).
11. Pu, T., Zhang, W. & Zhu, M. Engineering heterogeneous catalysis with strong metal–support interactions: Characterization, theory and manipulation. *Angewandte Chemie International Edition* **62**, e202212278 (2023).
12. Tang, H. *et al.* Classical strong metal–support interactions between gold nanoparticles and titanium dioxide. *Science Advances* **3**, e1700231.
13. Han, B. *et al.* Strong metal–support interactions between Pt single atoms and TiO_2. *Angewandte Chemie International Edition* **59**, 11824-11829 (2020).
14. Liu, S. *et al.* Ultrastable Au nanoparticles on titania through an encapsulation strategy under oxidative atmosphere. *Nature Communications* **10**, 5790 (2019).
15. Tang, M. *et al.* Facet-dependent oxidative strong metal-support interactions of palladium–TiO_2 determined by in situ transmission electron microscopy. *Angewandte Chemie International Edition* **60**, 22339-22344 (2021).
16. Wang, H. *et al.* Oxygen-saturated strong metal-support interactions triggered by water on titania supported catalysts. *Advanced Functional Materials* **33**, 2304303 (2023).
17. Li, J. *et al.* Tuning adsorbate-mediated strong metal-support interaction by oxygen vacancy: A case study in Ru/TiO_2. *Angewandte Chemie International Edition* **63**, e202407025 (2024).
18. Deleitenburg, C. & Trovarelli, A. Metal-Support Interactions in Rh/CeO_2, Rh/TiO_2, and Rh/Nb_2O_5 Catalysts as Inferred from CO_2 Methanation Activity. *Journal of Catalysis* **156**, 171-174 (1995).
19. van Deelen, T. W., Hernández Mejía, C. & de Jong, K. P. Control of metal-support interactions in heterogeneous catalysts to enhance activity and selectivity. *Nature Catalysis* **2**, 955-970 (2019).
20. Wang, T. *et al.* Nature of metal-support interaction for metal catalysts on oxide supports. *Science* **386**, 915-920 (2024).
21. Khivantsev, K. *et al.* Transforming ceria into 2D clusters enhances catalytic activity. *Nature* **640**, 947-953 (2025).
22. Weng, X. *et al.* Continuous hydrothermal syntheses of highly active composite nanocatalysts. *Green Chemistry* **13**, 850-853 (2011).
23. Stoyanov, E., Langenhorst, F. & Steinle-Neumann, G. The effect of valence state and site geometry on Ti $L_{3,2}$ and O K electron energy-loss spectra of Ti_xO_y phases. *American Mineralogist* **92**, 577-586 (2007).
24. Zhang, S. *et al.* Dynamical observation and detailed description of catalysts under strong metal–support interaction. *Nano Letters* **16**, 4528-4534 (2016).
25. Xu, J., Li, X., Liu, X. & Liu, J. EELS analysis of Ce valence state of SiO_2 supported CeO_2 nanoparticles, CeO_x nanoclusters and Ce single atoms. *Microscopy and Microanalysis* **26**, 728-730 (2020).

26. Xu, F. F. & Bando, Y. Valence evaluation of cerium ions in Ce-doped α-sialon by electron energy loss spectra. *Journal of Applied Physics* **89**, 5469-5472 (2001).
27. Borja-Urby, R., González-Vargas, O. A., Suárez-Toriello, V. A. & Herrera-Pérez, G. EELS post-processing and multiplet calculation for Ce^{4+}, Ce^{3+} valency determination in nanomaterials. *MRS Advances* **7**, 1032-1037 (2022).
28. Haruta, M. *et al.* Determination of elemental ratio in an atomic column by electron energy loss spectroscopy. *ACS Nano* **10**, 6680-6684 (2016).
29. Xiang, L. *et al.* In situ-formed tridentate Pd–SO_x coordination for sulfur-tolerant CO oxidation catalysis. *Environmental Science & Technology* **59**, 13073-13084 (2025).
30. Monai, M. *et al.* Restructuring of titanium oxide overlayers over nickel nanoparticles during catalysis. *Science* **380**, 644-651 (2023).
31. Tan, H., Wang, J., Yu, S. & Zhou, K. Support morphology-dependent catalytic activity of Pd/CeO_2 for formaldehyde oxidation. *Environmental Science & Technology* **49**, 8675-8682 (2015).
32. Bêche, E., Charvin, P., Perarnau, D., Abanades, S. & Flamant, G. Ce 3d XPS investigation of cerium oxides and mixed cerium oxide ($Ce_xTi_yO_z$). *Surface and Interface Analysis* **40**, 264-267 (2008).
33. Chen, J. *et al.* Reverse oxygen spillover triggered by CO adsorption on Sn-doped Pt/TiO_2 for low-temperature CO oxidation. *Nature Communications* **14**, 3477 (2023).
34. Zhang, T. *et al.* Simultaneously activating molecular oxygen and surface lattice oxygen on Pt/TiO_2 for low-temperature CO oxidation. *Nature Communications* **15**, 6827 (2024).
35. Li, W. *et al.* Zeolite-encaged isolated palladium redox centers toward sustainable wacker-type oxidations. *Journal of the American Chemical Society* **146**, 27600-27609 (2024).
36. Chen, W. *et al.* Role of the in-situ-formed surface (Pt–S–O)-Ti active structure in SO_2-promoted C_3H_8 combustion over a Pt/TiO_2 catalyst. *Environmental Science & Technology* **58**, 3041-3053 (2024).
37. Yoshii, K. Structural and magnetic studies of the lanthanide deficient perovskite $Ce_{2/3}TiO_3$. *Journal of Alloys and Compounds* **305**, 72-75 (2000).
38. Shan, C. *et al.* Recent advances of gaseous pollutant catalytic oxidation over precious metal catalysts with SO_2 exposure. *Environmental Science & Technology* **59**, 2348-2367 (2025).
39. Song, W., Su, Y. & Hensen, E. J. M. A DFT Study of CO Oxidation at the Pd–CeO_2(110) Interface. *The Journal of Physical Chemistry C* **119**, 27505-27511 (2015).
40. Lu, Y. *et al.* Enhancing activity and stability of Pd-on-TiO2 single-atom catalyst for low-temperature CO oxidation through in situ local environment tailoring. *Journal of the American Chemical Society* **146**, 28141-28152 (2024).
41. Liu, Y., Shan, Y. & Wang, Y. Novel simultaneous removal technology of NO and SO_2 using a semi-dry microwave activation persulfate system. *Environmental Science & Technology* **54**, 2031-2042 (2020).
42. Shen, Z. *et al.* Low temperature CO oxidation in sintering flue gas over Cu-Ce/AC catalysts: Effect of pretreatment with $KMnO_4$ on activity. *Catalysis Letters* **153**, 1726-1737 (2023).

43. Peshin, T., Sengupta, S. & Azevedo, I. M. L. Should India move toward vehicle electrification? Assessing life-cycle greenhouse gas and criteria air pollutant emissions of alternative and conventional fuel vehicles in India. *Environmental Science & Technology* **56**, 9569-9582 (2022).
44. Deng, J. *et al.* Catalyst deactivation in the abatement of atmospheric pollutants: Origin, resistance, and regeneration. *Chemical Reviews* **125**, 11260-11357 (2025).
45. Chen, L. *et al.* Asymmetric oxygen vacancy-enriched Mn_2O_3@CeO_2 for NO oxidation with excellent low-temperature activity and boosted SO_2-resistance. *Applied Catalysis B: Environmental***340**, 123202 (2024).

Figures

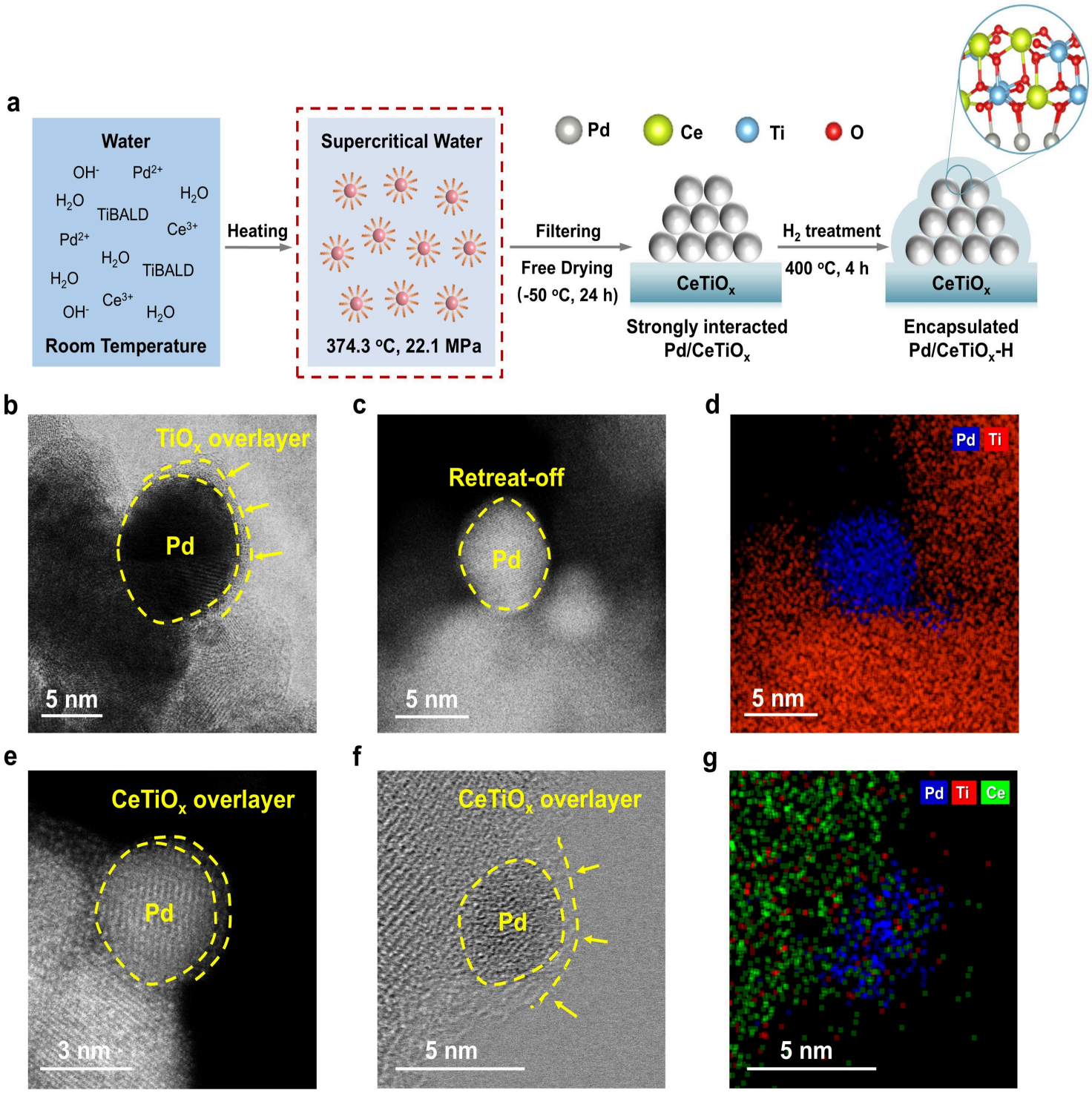


Figure 1

Stable Ce–Ti overlayer under oxidative and humid conditions. Schematic diagram for preparing $Pd/CeTiO_x$–H (a), AC–TEM images of Pd/TiO_2–H (b), treated Pd/TiO_2–H (c), $Pd/CeTiO_x$–H (e), and treated $Pd/CeTiO_x$–H (f), EDS mapping images of treated Pd/TiO_2–H (d) and $Pd/CeTiO_x$–H (g). Treatment condition: 200 ^{o}C, 20 vol% O_2, 5 vol% H_2O, and 2 h.

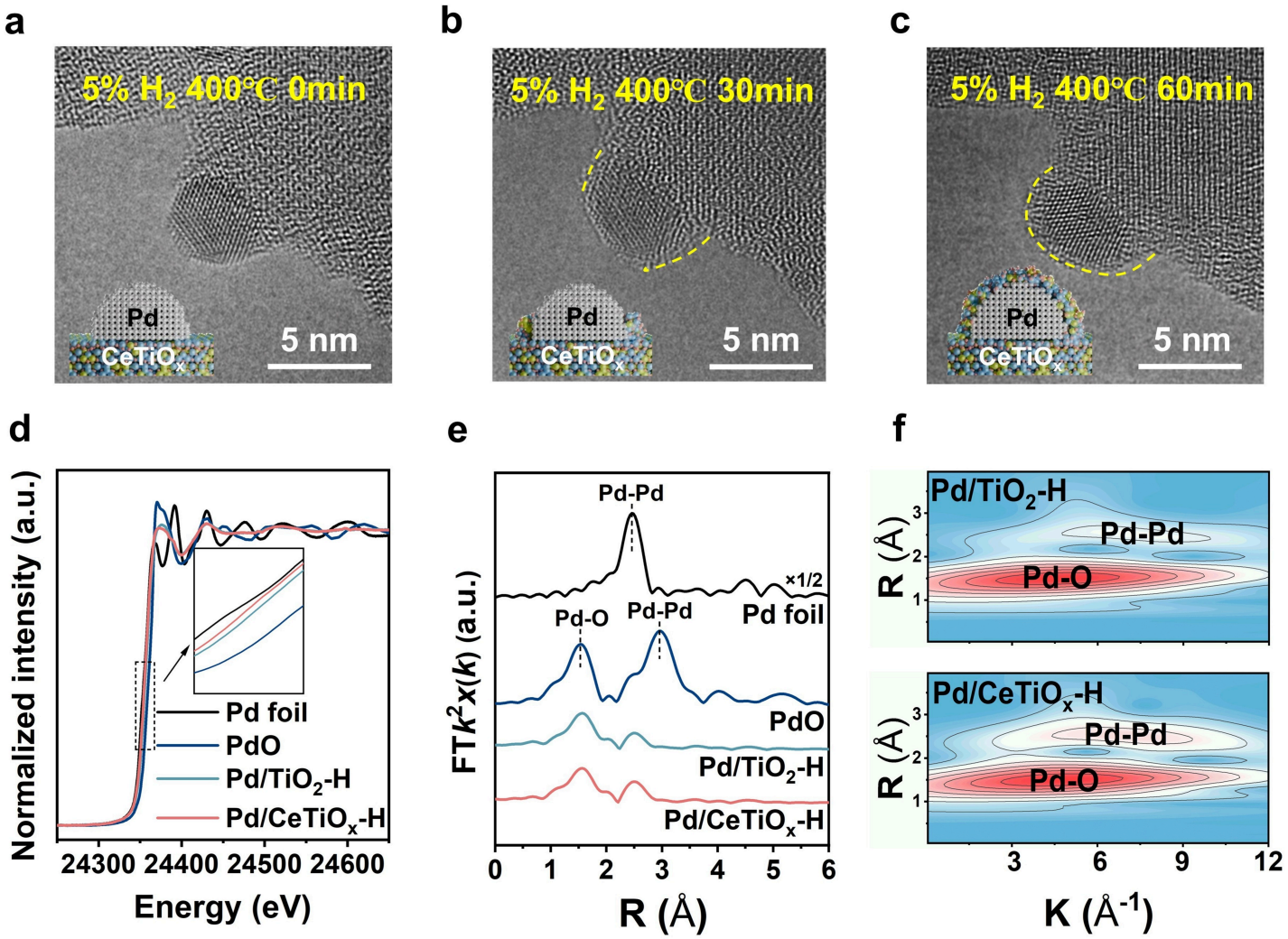


Figure 2

***In situ* formation and structure of Ce–Ti overlayer.** Sequential *in situ* environmental TEM images show the structure evolution of Pd/$CeTiO_x$–H in 5 vol% H_2 (gas pressure 5 kPa, balanced with Ar) at 400 °C (a–c), normalized Pd K–edge X–ray absorption near–edge structure (XANES) spectra (d), Fourier transform of extended X–ray absorption fine structure (FT–EXAFS) spectra of Pd/TiO_2–H, Pd/$CeTiO_x$–H, Pd foil, and PdO (e), Wavelet transform (WT) of EXAFS spectra of Pd/TiO_2–H and Pd/$CeTiO_x$–H (f). R represents the average distance between atoms, while k represents the wave vector of the photoelectron.

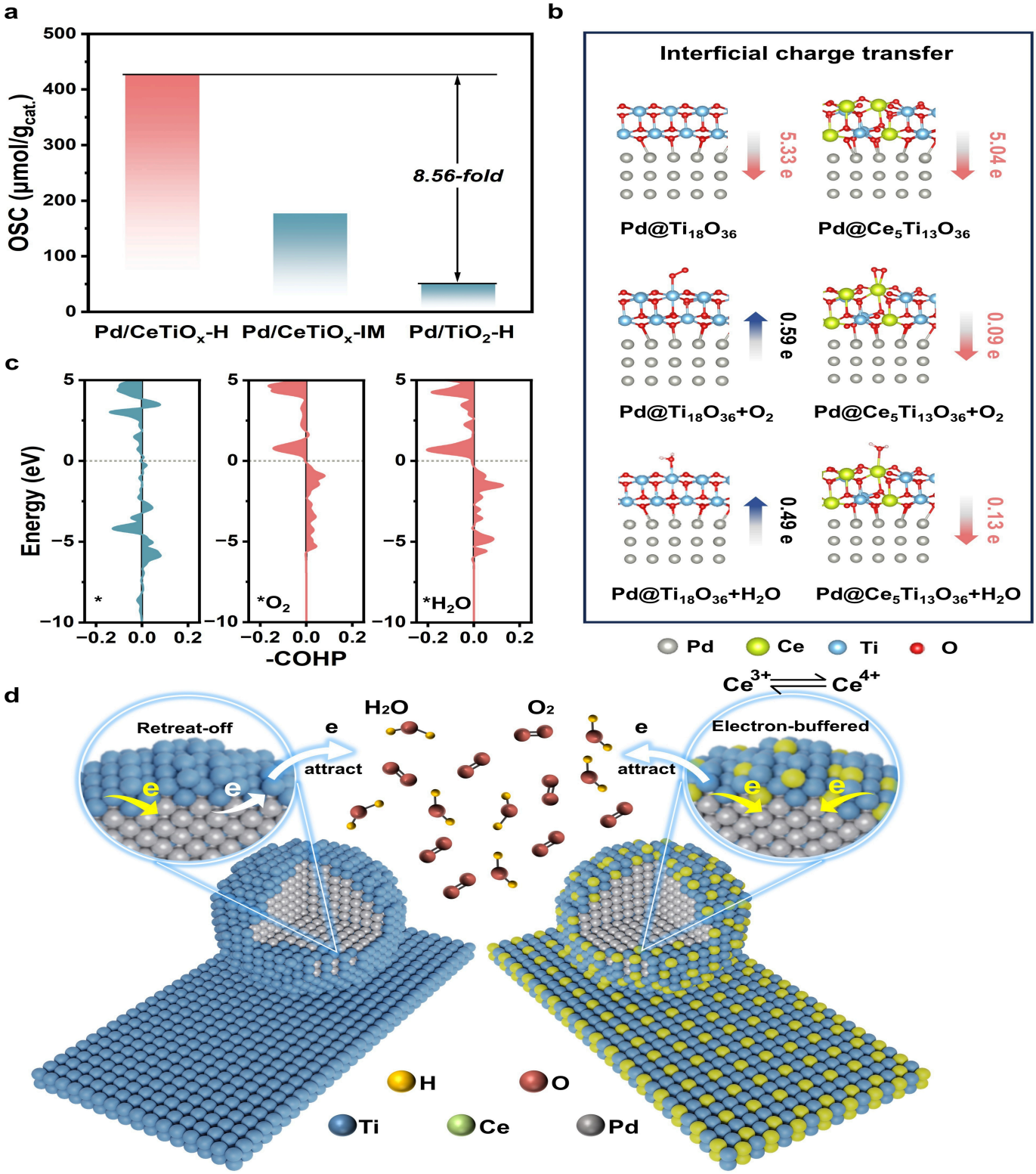


Figure 3

Experimental and theoretical insights into the origin of stable Ce–Ti overlayer. OSC of Pd/CeTiO$_x$–H, Pd/CeTiO$_x$–IM, and Pd/TiO$_2$–H (a), bader charge of encapsulated–Pd models with Ti$_{18}$O$_{36}$ and Ce$_5$Ti$_{13}$O$_{36}$ overlayers with/without adsorption of O$_2$ and H$_2$O (b), –COHP of Pd–Ce in encapsulated–Pd

models with $Ce_5Ti_{13}O_{36}$ overlayers after adsorption of O_2 and H_2O (c), scheme showing electron–buffered mechanism under humid and oxidative conditions (d).

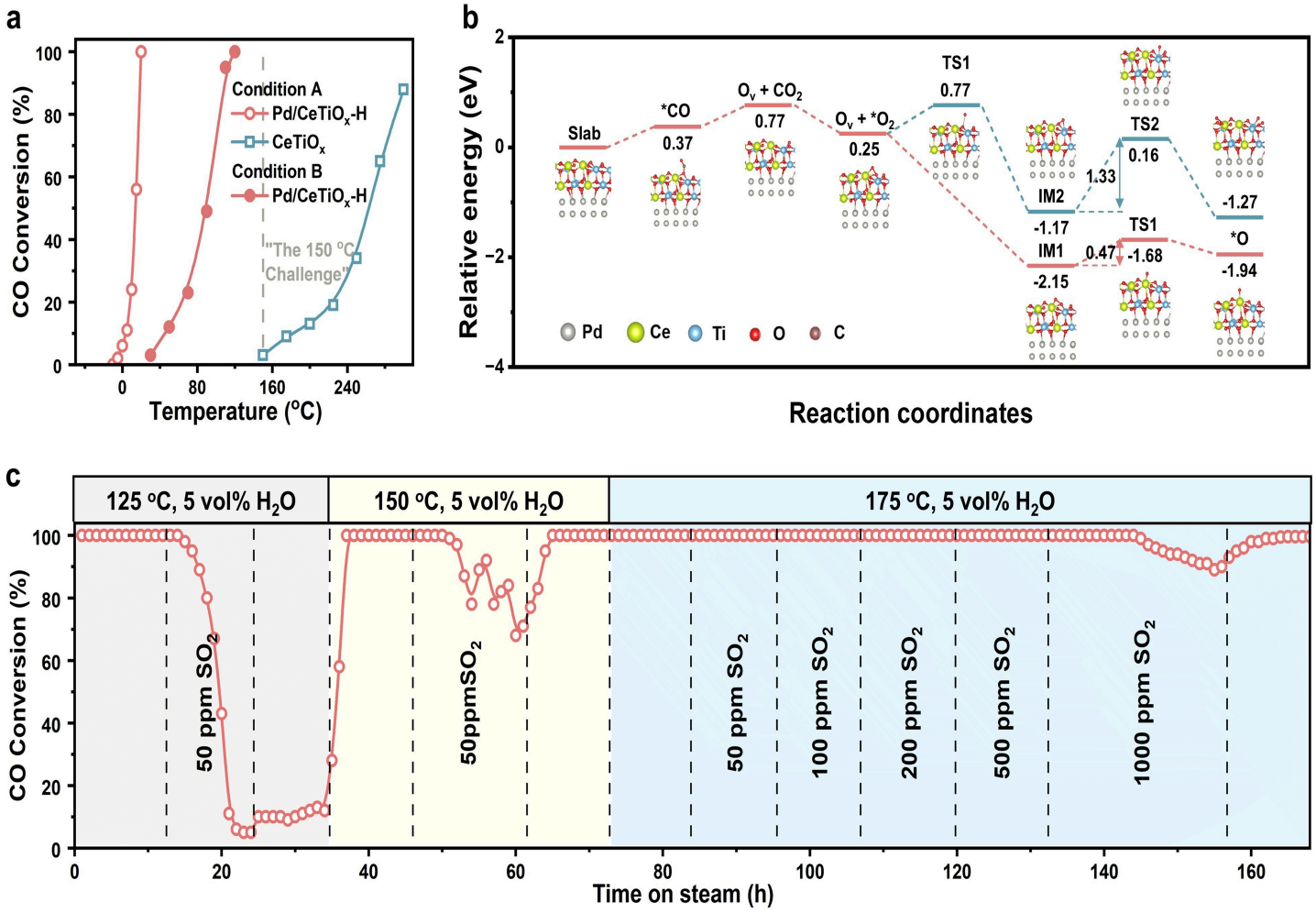


Figure 4

Catalytic tests in CO oxidation. CO conversions over $Pd/CeTiO_x$–H and $CeTiO_x$ (condition A: 2500 ppm CO, 10 vol% O_2, 20000 $mL{\cdot}g^{-1}{\cdot}h^{-1}$, condition B: 4000 ppm CO, 10 vol% O_2, 200000 $mL{\cdot}g^{-1}{\cdot}h^{-1}$ (a), relative energy profiles for the CO catalytic oxidation pathway on $Pd@Ce_5Ti_{13}O_{36}$ (b), CO conversion with time on stream at 125–175 °C with 5 vol% H_2O and the alternative treatment of 50–1000 ppm SO_2 (c).

Supplementary Files

This is a list of supplementary files associated with this preprint. Click to download.

- NSsupplementaryclean.docx